Edinburgh Research Explorer

Operando DRIFTS-MS Investigation on Plasmon-Thermal Coupling Mechanism of CO2 Hydrogenation on Au/TiO2: The Enhanced Generation of Oxygen Vacancies

Operando DRIFTS-MS Investigation on Plasmon-Thermal Coupling Mechanism of CO_2 Hydrogenation on Au/TiO$_2$: The Enhanced Generation of Oxygen Vacancies

Ke Wang,[1] Mengyu Cao,[1] Jiangbo Lu,[2] Ying Lu,[1] Cher Hon Lau,[1] Ying Zheng,[3] and Xianfeng Fan[1,*]

1. Institute for Materials and Processes, School of Engineering, the University of Edinburgh, Edinburgh, EH9 3FB, Scotland.

2. School of Physics and Information Technology, Shaanxi Normal University, Xi'an, 710119, China.

3. Department of Chemical and Biochemical Engineering, Western University, London, Ontario, N6A 5B9, Canada.

* Corresponding author: x.fan@ed.ac.uk (Xianfeng Fan)

1   **ABSTRACT:** Using solar energy to promote the thermocatalytic CO_2 conversion is a promising

2   way to reduce the energy consumption and increase the sustainability. Au/TiO_2 is known for its

3   good catalytic activity in both thermo- and photo- catalytic CO_2 conversion, however both the

4   reaction mechanisms in dark and in photo-thermo coupled reaction condition remain unclear. In

5   this work, the operando isotope-labelled spectroscopic and computational analyses are combined

6   to clarify these mechanisms. The redox mechanism that CO_2 direct dissociation at the oxygen

7   vacancy (V_O) is found as the main reaction pathway of CO_2 hydrogenation over Au/TiO_2. The

8   plasmonic enhancement mechanism is proven to be the hot electrons facilitated V_O generation at

9   interface. The clear understandings of reaction pathway and plasmonic enhancement mechanism

10   are helpful for the future design of photo-thermal CO_2 conversion catalysts.

11

1   Introduction

Environmental effects of CO_2 emission have drawn significant attentions from the whole society [1]. Besides CO_2 emission control, the technology that converts CO_2 to profitable products is believed as an important method to achieve the carbon neutrality. It is pivotal to use renewable energy to drive the CO_2 conversion as much as possible to fulfil the initiate. The conventional photocatalysis shows slow reaction rate and fails to meet the requirements of practical implementation. Therefore, it is promising to combine the photocatalysis and thermocatalysis together for a synergistic effect on boosting the CO_2 conversion [2-5].

For CO_2 hydrogenation, the reverse water gas shift (RWGS) reaction is often the first step of CO_2 conversion. The CO product is an important feedstock for the synthesis of more valuable chemicals. Au/TiO_2 shows good thermocatalytic CO_2 hydrogenation activity [6, 7] and is also known as one of the best plasmonic photocatalysts for CO_2 conversion [8, 9]. Therefore, the Au/TiO_2 is a promising catalyst for plasmon-enhanced thermocatalytic CO_2 conversion application. However, the reaction mechanism for RWGS reaction over Au/TiO_2 in dark is still under debate due to insufficient investigations. The plasmonic enhancement mechanism under photo-thermo coupled condition is even less understood. For RWGS reaction mechanism in dark, the proposed ones in literature can be generally divided into two categories: redox and associative mechanisms. The redox mechanism includes the direct CO_2 reduction to CO by the reduced catalyst surface or metal clusters. For example, Wang et al. [10] demonstrated the CO_2 directly dissociated on Au/CeO_2. Liu et al. [11] proved that the CO_2 spontaneously dissociated into CO under the co-effects of Cu(I) and reduced TiO_{2-x}. The indispensable role of V_O in Au/TiO_2 is highlighted in literature [6, 12]. On the other hand, the associative pathway is characterised by the

1 involvement of key reaction intermediates including carbonate[6, 13, 14], formate [15, 16] and

2 carboxyl (COOH*, hydroxycarbonyl) [17-19]. For photo-enhancement mechanism, most of the

3 current researches focus on the demonstration that light irradiation can enhance the thermocatalytic

4 reaction rate or alter the product selectivity [2, 20-25], however the mechanism underpinning the

5 enhancement is still ambiguous. Clear understanding of the photo-enhancement mechanism is

6 indispensable for developing more efficient catalysts with desired product selectivity specific for

7 photothermal reaction condition. Some of the enhancement mechanism investigations [9, 26, 27]

8 focus on the reaction happens on the plasmonic metal cluster alone with little consideration of the

9 contribution of the reducible oxide supports. Other works propose the plausible mechanisms via

10 indirect evidences. For example, Upadhye et al. [17] reported the localised surface plasmon

11 resonance (LSPR) enhanced CO_2 hydrogenation to CO in reaction rate. And the mechanism of the

12 photo-enhancement was proposed to multiple reaction steps including the carboxyl (COOH*)

13 decomposition, hydroxyl hydrogenation and desorption of the H_2O^* and CO^*. Liu et al. [28]

14 suggested that the plasmonic enhancement mechanism was the electron-assisted CO_2 dissociation

15 to O$^\bullet$ radical. Therefore, more investigations are needed to present direct evidences on elucidation

16 of the CO_2 reduction mechanism under photo-thermo coupled reaction condition. And the light-

17 induced enhancement cannot be unravelled without a clear understanding of the reaction pathway

18 in dark.

19

20 Herein, the reaction mechanisms of RWGS on Au/TiO_2 under thermocatalytic and plasmon-

21 enhanced thermocatalytic reaction conditions are investigated via *operando* diffuse reflectance

22 infrared fourier-transform spectroscopy coupled with mass spectroscopy (*operando* DRIFTS-MS),

23 *ex-situ* electron paramagnetic resonance (EPR) spectroscopy, steady-state isotope transient kinetic

analyses (SSITKA) and kinetic isotope effects (KIE) measurements. The CO_2 directly dissociates at the V_O site, the redox pathway, is proven as the main reaction mechanism of CO_2 conversion over Au/TiO_2 under both thermal and photo-thermo coupled reaction condition. Both experimental and theoretical evidences indicate that the plasmon-excited hot electrons in Au inject into TiO_2 support and facilitate the V_O generation, which is the plasmonic enhancement mechanism.

2　Experimental

2.1　Materials

Isotopic gases including Deuterium (99.8% atom D_2) and $^{13}CO_2$ (99% atom 13C) are supplied by the Sigma-Aldrich. High purity synthetic Air (zero grade), Ar (CP grade), H_2 (zero grade), CO (research grade) and CO_2 (CP grade) used in the experiments are all supplied by BOC limited, UK. Aeroxide® P25 with ~80% anatase and ~20% rutile composition is used as TiO_2 support. The P25 and formic acid (reagent grade, stabilized by 2.5% water) are supplied by Sigma Aldrich. $HAuCl_4·3H_2O$ (ACS reagent) and urea (99%) are purchased from ACROS organics. Ultrapure water is used through the experiments.

2.2　Catalysts synthesis

Au/TiO_2 catalysts were synthesized following the standard deposition-precipitation (DP) method with urea. 1.5 mmol $HAuCl_4·3H_2O$ and 150 mmol urea were dissolved in 100 mL under vigorous stirring. 1 g of TiO_2 powder was dispersed inside the solution and the container was covered with aluminium foil blocking the ambient light. Then the beaker was transferred into an oil bath and heated up to 80 ^oC with continuous stirring. The solution was kept at 80 ^oC for 5 h. Before cooling down to room temperature, the catalyst powder was vacuum-filtrated and washed with water for 8

1 times to remove residual Cl$^-$ ions. The filtered cake was dried inside a vacuum oven at 60 °C

2 overnight and then calcinated at 400 °C for 2 h inside a muffle furnace. The ramping rate for the

3 calcination was set to 1 °C min^{-1}.

4

5 **2.3   Catalysts characterization**

6 The crystalline structure of the prepared catalysts was characterized by an X-ray diffractometer

7 (XRD, Brucker D2 Phaser). The oxidation states of both Au and TiO$_2$ were characterized by an X-

8 ray photoelectron spectrometer (XPS, Kratos Axis Ultra DLD). Electron paramagnetic resonance

9 (EPR) spectra were measured with an EPR spectrometer (Brucker A3000) at 77 K with a

10 microwave frequency of 9.857 ± 0.002GHz. The morphology of the catalyst powder was analysed

11 with an aberration-corrected transmission electron microscope (TEM, JEOL ARM200F) using

12 high-angle annular dark field scanning transmission electron microscope (HAADF-STEM) mode.

13 The Au nanoparticle size distribution curve was calculated by measuring 160 nanoparticles. The

14 specific surface area (SSA) of Au/TiO$_2$ was characterized via N$_2$ sorption isotherm at 77 K

15 (Quantachrome Autosorb iQ). The loading of Au was measured using inductively coupled plasma

16 optical emission spectroscopy (ICP-OES) method. 20 mg of catalyst was dissolved using 10 mL

17 aqua regia inside the PTFE autoclave at 80 °C for 4 h. The 10 mL aqua regia was further diluted

18 to 500 mL with volumetric flask. The liquid analyte was then extracted by an autosampler of the

19 ICP-AES Spectrometer (Varian Vista-Pro). The ultraviolet-visible diffuse reflectance

20 spectroscopy analyses (UV-Vis DRS) were conducted using the praying mantis setup (Harrick) as

21 an accessory to a UV-Vis spectrophotometer (Shimadzu UV-3600 plus). BaSO$_4$ power was packed

22 into the sample cup for background spectrum collection.

23

2.4 Catalytic performance evaluation

The commercial praying mantis high temperature reactor was used as the reactor to ensure the consistent condition with the *in-situ* spectroscopy analyses. Au/TiO_2 catalyst powder was first pelletised and sieved into the size between 63-125 microns according to the standard palletisation procedure. 10 mg powder was packed into the reactor every time. The temperature of the reactor was calibrated for the whole reaction temperature range with an external thermocouple (0.5 mm in diameter) immersed inside the powder and a thermometer (RS Pro) was used to read the real temperature. CO_2 (1 sccm), H_2 (4 sccm) and Ar (25 sccm) was controlled by mass flow controllers (Omega engineering) and mixed before introduced into the reactor. The inlet and outlet gas line of the reactor was kept at 130 ^{o}C to prevent condensation. The products of reaction were analysed with a gas chromatography (GC, Shimadzu 2010 Plus) equipped with a thermal conductivity detector (TCD) and a flame ionization detector (FID). A carbon molecular sieve micro-packed column (Restek ShinCarbon ST Column) was used to separate the gaseous analytes for quantitative analyses. The gas flows are regularly calibrated with an electronic gas flowmeter (Agilent). External green (520 nm) and blue (445 nm) LED lights were introduced into the reactor from the front quartz window via an optical liquid guide. The power intensities of green and blue light are measured to be 250.1 and 320 mW cm^{-2} respectively using a thermopile optical power meter (Thorlabs, PM601).

2.5 *Operando* DRIFTS-MS analyses

The operando diffuse reflectance infrared Fourier-transform spectroscopy coupled with a mass spectrometer (DRIFTS-MS) was used to *in-situ* analyse the chemical species on the surface during the reaction. The praying mantis (Harrick) mirror set with the reactor was installed inside an

1 infrared (IR) spectrometer (Shimadzu, IRTracer-100) with the gas supplying system described in

2 the catalytic performance evaluation section. Buffering gas lines with Ar (30 sccm) or Air (30

3 sccm) are also included and controlled with mass flow controllers. The buffering gas lines and the

4 reaction gas lines are switchable with a four-way valve to ensure a fast and reliable exchange. A

5 liquid nitrogen cooled mercury cadmium telluride (MCT) detector was used to detect the IR signal

6 from 1000 to 4000 cm^{-1} with the resolution of 4 cm^{-1}. All the effluent gases during the *operando*

7 experiments were monitored with an on-line mass spectrometer (MS, QGA Hiden Analytical).

8

2.6 SSITKA-MS and KIE analyses

10 Steady-state isotope transient kinetic analyses (SSITKA) were conducted using the same setup

11 with *operando* DRIFTS-MS. The stable isotope-labelled $^{13}CO_2$ was used during the SSITKA-MS

12 experiments. The flow of $^{13}CO_2$ was controlled with a mass flow controller and checked regularly

13 to keep it the same to the unlabelled $^{12}CO_2$ flow with an electronic gas flowmeter. The switch

14 between $^{12}CO_2$ and $^{13}CO_2$ gas flow was achieved by a four-way valve. The surface intermediates

15 were observed with the IR spectrophotometer and gaseous effluent from the reactor was monitored

16 by a MS.

17

18 The kinetic isotope effects were measured using the same setup with the catalytic performance

19 evaluation. Deuterium gas (D_2) was used to replace the H_2 during the reaction and the gas flow of

20 4 sccm was calibrated using the electronic gas flowmeter to ensure the same flow with H_2 used in

21 the catalytic performance evaluation. The products were quantitatively measured by a GC.

22

2.7 Theoretical calculation

1 The theoretical calculation based on density function theory (DFT) was conducted using the

2 Quantum Espresso package [29, 30]. The exchange-correlation energy and potential are described

3 at general gradient approximation (GGA) level with Perdew-Burke-Ernzerhof (PBE) functional

4 [31]. The potentials of nuclei and core electrons are approximated with ultrasoft pseudopotentials

5 (USPP) in "GBRV" library [32]. The kinetic energy cutoff for plane-waves and charge

6 density/potential were 45 and 450 Ry respectively according to convergence test results. A

7 gaussian smearing with 0.01 Ry width was used in the calculation to accelerate the convergence.

8 The energy and force convergence criteria for the structure relaxation were set to be 1×10^{-4} Ry and

9 1×10^{-3} Ry Bohr^{-1} respectively. Spin-polarization was considered for all the calculation in this work.

10 Bulk anatase TiO_2 and Au were calculated with their primitive cells with $6 \times 6 \times 6$ and $16 \times 16 \times$

11 16 k-points meshes, respectively. A Hubbard $U_{eff} = 4.2$ eV [33-35] correction was added to Ti 3d

12 orbitals in a simplified form [36] to have a better description of on-site Coulomb interaction. For

13 small molecule adsorption calculation, the unphysical dipole potential due to periodic boundary

14 condition was corrected along Z-direction. The van de Waals interaction is corrected using the

15 empirical Grimme-D3 method [37]. The transition states were searched with the climbing image

16 nudged elastic band (CI-NEB) method [38] with the convergence threshold of 0.03 eV Å^{-1}. All the

17 plots related to DFT calculation were generated with the VESTA [39]. The COHP bonding

18 analyses were conducted with the Lobster code [40] with the structure optimised with projected

19 augmented-wave (PAW) pseudopotentials from PSLibrary [41].

20

3 Results and discussion

3.1 Catalysts characterization

The catalysts used in this work is Au/TiO_2 with Au loading of 2.76 wt%, which is determined by inductively-coupled plasma optical emission spectrometry (ICP-OES). The Au particles size is measured with high-angle angular dark-field scanning transmission electron microscope (HAADF-STEM) images with typical images shown in Figure S1(a, b) in supplementary information (SI-Section 1). In the HAADF-STEM images, the TiO_2 supports (P25) exhibit darker contrast comparing with Au nanoparticle due to its lower atomic weights. The size of the TiO_2 powder is ~20 nm. The Au nanoparticles, showing brighter contrast, homogeneously distribute on the TiO_2 surface. The mean Au particle diameter is calculated to be 4.79±2.0 nm based on the measurement of 160 Au nanoparticles in total (Figure S1(c)). Additional physical characterizations and discussions including powder X-ray diffraction (XRD), X-ray photoelectron spectroscopy (XPS), N_2 sorption and ultraviolet-visible light diffuse reflectance spectroscopy (UV-Vis DRS) analyses are described in SI-Section 1 and shown in Figure S2(a-d) respectively. In summary, the 2.76wt% Au/TiO_2 catalysts used in this work is a typical Au/TiO_2 catalyst similar to those reported in many former works for either photo- or thermo- catalytic applications [6, 17, 42-45]. The characterization results prove the Au/TiO_2 is a suitable catalyst for plasmon-enhanced thermocatalytic CO_2 hydrogenation. It also ensures the mechanism investigation results of this work of general interests to the catalysis research community.

## 3.2 The plasmon-enhanced CO_2 hydrogenation performance at different temperatures

The CO is the only product detected and the production rates (rCO) under different reaction conditions are plotted in Figure 1(a). It shows that the both green and blue light-induced plasmonic hot carriers do enhance the reaction rate for faster CO production at all temperatures investigated.

1 At 200 °C, the CO production rates reach 0.22, 0.70 and 0.30 µmol g_{cat}^{-1} s^{-1} at dark, green and blue

2 light irradiation conditions. The reaction rate at 200 °C under dark is similar to the reported value

3 of typical Au/TiO$_2$ catalyst [6, 20]. The green-light induced plasmon significantly enhances the

4 reaction rate to ~ 318% of the dark reaction. Different from the green-light enhancement, the blue-

5 light is less effective in promoting the reaction rate, which shows only 136% promotion comparing

6 with dark reaction condition. It is noted that the net plasmon-induced CO production rate ($r_{CO\text{-}green}$

7 $- r_{CO\text{-}dark}$ or $r_{CO\text{-}blue} - r_{CO\text{-}dark}$) shows a monoclinic increase with temperature rise. However, the

8 plasmonic enhancement ratios decline. The apparent E_a of reaction on Au/TiO$_2$ under dark is

9 calculated to be 46±4.7 kJ mol^{-1}, which is similar to literature [6, 17]. The blue and green light

10 induced plasmon-enhanced RWGS reaction exhibit a lower E_a of 44.0±2.9 and 37.0±0.9 kJ mol^{-1},

11 respectively (Figure S3), which suggests the plasmonic hot electrons help to lower the kinetic

12 energy barrier of the rate determining step (RDS). Additionally, the correlation between light

13 intensity and plasmon-enhancement is also investigated. The CO production rates are plotted as a

14 function of green light intensity at different reaction temperature in Figure 1(b). Note that the CO

15 production rate increases linearly with the light intensity. The high linearity suggests the hot-

16 electrons rather than simple light induced thermal effects are likely to be responsible for the

17 reaction rate enhancement [46]. Further discussions on the quantum efficiency (QE) and the hot

18 electron enhancement are presented in SI-Section 2. It is found the QE also increases at higher

19 reaction temperature. It is also of interest to investigate the catalytic activity as a function of time.

20 As shown in Figure S4, the Au/TiO$_2$ shows an activation process within the first 20 min of time

21 on stream and becomes stable after 120 min. The activation process is likely derived from the V_O

22 accumulation at first 20 min and reaching equilibrium concentration after 120 min. In summary,

23 these experimental results demonstrate that the light-induced plasmonic enhancement positively

1 correlates with both temperature and light intensity. The apparent activation energy can be

2 significantly reduced by coupling light to thermocatalytic RWGS reaction. It is also worth

3 investigating the catalytic performance of pristine TiO_2 support under dark and green light

4 irradiation as control experiments. The corresponding results are shown in Figure S5. The pristine

5 TiO_2 shows negligible activity at all temperatures under dark. The green light shows small

6 enhancements on CO production rate only at temperature higher than 300 °C. This result is

7 rationalized by the weak absorption of green light when V_O energy level is created within the

8 bandgap of H_2-reduced TiO_2 [47-49]. The net light-induced CO production rate ($r_{CO\text{-}green} - r_{CO\text{-}dark}$)

9 over pristine TiO_2 at 500 °C is measured to be 0.51 μmol g_{cat}^{-1} s^{-1}, which is only 14.5% of the net

10 light-induced CO production rate of 3.52 μmol g_{cat}^{-1} s^{-1} over Au/TiO_2. The more pronounced light-

11 enhancement is attributed to the plasmonic effects of Au nanoparticles. The roles of Au

12 nanoparticles in the thermo-photo coupled CO_2 hydrogenation reaction can be summarized to three

13 aspects: (1) facilitating H_2 dissociation; (2) facilitating V_O generation and (3) producing plasmonic

14 hot electrons [50-52].

15
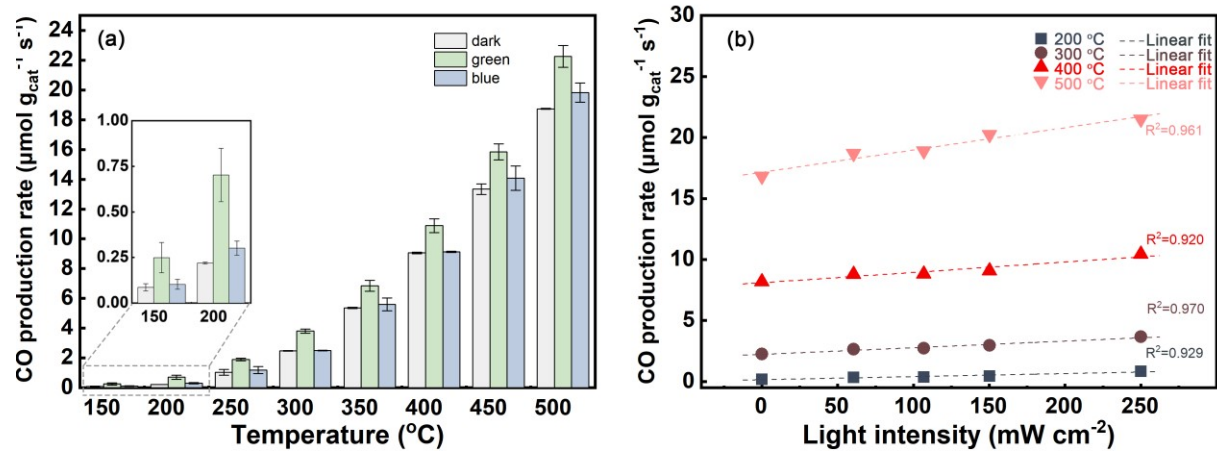
16

17 Figure 1. (a) The CO production rates of Au/TiO_2 at temperature ranging from 150 to 500 °C under
18 dark, green light and blue light irradiation. The inset is the magnification of columns at 150 and

12

200 °C. (b) CO production rates at different green light power densities and the corresponding linear regression analyses.

3.3 Enhanced V_O formation elucidated by *ex-situ* EPR analyses

The *ex-situ* EPR measurements providing a direct understanding of V_O concentration in Au/TiO_2 are used to elucidate the effects of light irradiation on V_O creation. The 4 groups of catalysts are treated at 200 °C for 1 h to reach the equilibrium at the different light irradiation conditions and atmospheres: (i) dark/air, (ii) dark/reaction atmosphere, (iii) green light/reaction atmosphere and (iv) blue light/reaction atmosphere, respectively. As shown in Figure 2(a), the peaks at g = 2.004 in EPR spectra are assigned to V_O in Au/TiO_2 [53-55]. To achieve a quantitative comparison of V_O concentration [56], the microwave absorbances peaks at 2.004 are double-integrated and the normalised peak areas are plotted in Figure 2(b). Note that the Au/TiO_2 under green light irradiation and reaction atmosphere shows the highest V_O concentration. Comparatively, the V_O concentration of Au/TiO_2 under dark condition with reaction atmosphere is only 48.6% of the counterpart under green light irradiation. The control group of Au/TiO_2 treated under flowing air in dark at the same temperature exhibits the lowest V_O concentration of 34.0%. The non-zero V_O concentration is because the TiO_2 is a n-type semiconductor possessing intrinsic V_O in the lattice even annealed in air [57]. The EPR analyses results prove that more V_O is generated under plasmonic enhancement comparing with pure thermocatalytic reaction condition.
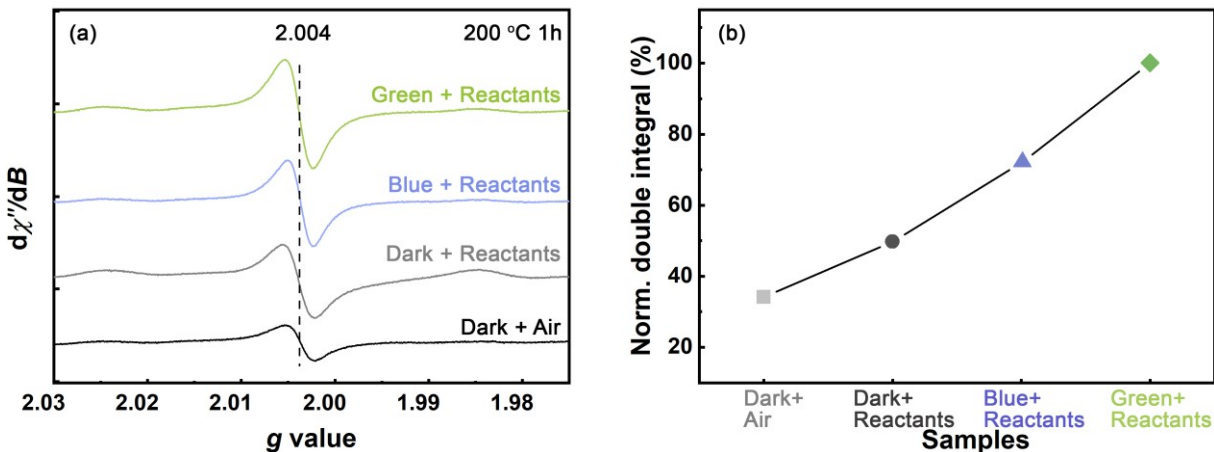
Figure 2. (a) EPR spectra of samples treated at different light irradiation conditions and atmospheres at 200 °C for 1h. (b) The corresponding double-integrals of ESR peak at g=2.004 at different atmosphere and light irradiation conditions; the integrals are normalized to the maximum value. The dark, blue and green represent the no irradiation, green light and blue light irradiation conditions, respectively. The reactants atmosphere is the same to the atmosphere during the catalytic performance evaluation.

3.4 *In-situ* spectroscopy analysis of reaction mechanism

3.4.1 Steady-state *operando* DRIFTS-MS analysis

In order to elucidate and compare the RWGS reaction pathways under dark and plasmon-enhanced reaction conditions, the *operando* DRIFTS-MS measurements are conducted at reaction temperature of 200 °C in dark for 30 min, which is followed by an instant switch-on of green light for another 30 min (Figure 3). To ensure a reliable IR assignment for peaks in our work, $^{12}CO_2/^{13}CO_2$ adsorption and formic acid adsorption control experiments are conducted on this specific Au/TiO$_2$ catalyst (details in SI-Section 3). The corresponding IR spectra and deconvolutions are illustrated in Figure S6 & S7 and the peak assignments are summarized in Table S2 & S3.

As shown in Figure 3(a), the time-resolved DRIFT spectra of Au/TiO_2 under dark at 200 °C show
that the steady state is reached within 30 min. 4 different species are observed on the surface: H_2O,
carbonate, bicarbonate and formate. The peaks at 1620 cm^{-1} are assigned to adsorbed H_2O^* [58]
due to the consistent peak position in $^{12}CO_2$ and $^{13}CO_2$ adsorption spectra (Figure S7). The peaks
centred at 1560, 1338 cm^{-1} are assigned to the asymmetric and symmetric stretching of O-C-O
(v_{as}(O–C–O) and v_s(O–C–O)) respectively in bidentate carbonate (b-CO_3^*) group. Similarly, the
v_{as}(O–C–O) and v_s(O–C–O) of monodentate carbonate (m-CO_3^*) group exhibit the corresponding
peaks at 1535, 1510 and 1382 cm^{-1} [59-63]. In the case of bicarbonate, the peaks emerged at 1455,
1440 and 1424 cm^{-1} are assigned to either monodentate or bidentate bicarbonate (m-HCO_3^* or b-
HCO_3^*) on the surface [61-64]. Formate is featured by its C-H vibration peaks at 2955 and 2887
cm^{-1} [65-68]. Additionally, the peaks at 1553, 1360 cm^{-1} are assigned to the asymmetric and
symmetric stretching of O-C-O (v_{as}(O–C–O) and v_s(O–C–O)) in formate species ($HCOO^*$). After
achieving the steady state of surface species under dark reaction condition, the green light is
switched on to provide a plasmon-enhanced reaction condition. It can be seen from Figure 3(b)
that the CO production rate indicated by MS signal increases as soon as the green light is turned
on, which confirms the existence of plasmon-enhancement. After green light switch-on, the
evolution of characteristic peaks for each species are normalized and plotted as a function of time
(Figure 3(c)). The most significant difference after the green light switch-on is the peak intensity
drop of H_2O^* (1620 cm^{-1}) and HCO_3^* (1455, 1440, 1424 cm^{-1}). The peaks corresponding to $HCOO^*$
and CO_3^* remain stable under light irradiation. In summary, $HCOO^*$, CO_3^* and HCO_3^* surface
species are observed during the reaction. The green light irradiation doesn't introduce extra
adsorbed species on the surface, while the adsorbed H_2O^* are strongly depressed by light
irradiation. Note that the peak at 3412 cm^{-1} is relatively stable, which is very different from

15

1 molecular H_2O^* at 1620 cm^{-1}. In literature, the 3412 cm^{-1} peak assignment is an unresolved

2 question, which is either assigned to OH^* or H_2O^*. A very recent combined experiment and

3 simulation work by Mino et al. [69] suggested the peak at around ~3420 cm^{-1} was derived from

4 H-bonded OH^* group. Considering the different behaviours of peaks at 3412 and 1620 cm^{-1}, the

5 3412 cm^{-1} peak might be either OH^* or H_2O^* adsorbed at site far away from Au/TiO$_2$ interface,

6 which are less affected by plasmonic effects.

7

8
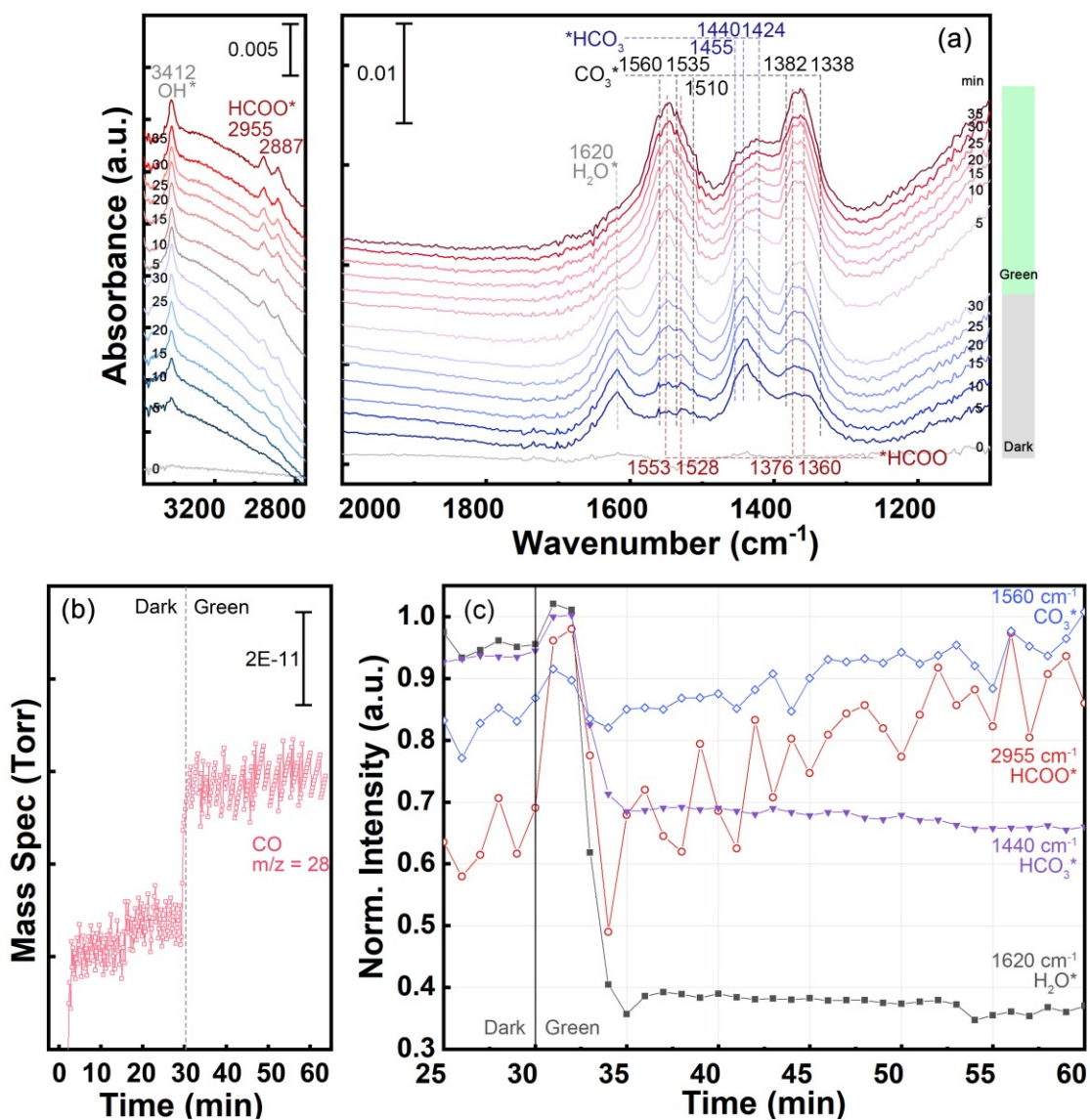
Figure 3. (a) Time-resolved operando-DRIFT spectra and corresponding (b) CO MS signal (m/z =28) of Au/TiO$_2$ interaction with reaction gas mixture (CO$_2$ 1 sccm, H$_2$ 4 sccm, balanced with 25 sccm Ar) at 200 °C. The green light is switched on at 30 min after reaction reaches steady state under dark. (c) The time-resolved IR peak intensity changes representing surface species of CO$_3$*, HCOO*, HCO$_3$* and H$_2$O*. The IR peak intensities are normalized to their individual maximum.

3.4.2 Reaction intermediate analysis by SSITKA-MS

To distinguish the observed species in in-situ DRIFTS-MS experiments as reaction intermediates or spectators, the SSITKA-MS experiments can provide more convincible evidences. As shown in Figure 4(a, b), the IR spectra of Au/TiO$_2$ under dark reaction condition at 200 °C reach steady-state within 60 min. The peaks stabilized on the surface are assigned to HCOO*, HCO$_3^*$, CO$_3^*$ respectively, which are consistent to Figure 3(a). At 60 min, the ^{12}CO$_2$ is instantly switched to ^{13}CO$_2$ and the IR peaks of CO$_3^*$ and HCO$_3^*$ exhibit a gradual decrease. It is noticed that the H^{12}COO* at 2955 and 2887 cm^{-1} shows no shift or decrease after switching from ^{12}CO$_2$ to ^{13}CO$_2$ within 0.5 h. The effluent ^{12}CO/^{13}CO is monitored via a mass spectrometer and the results are shown in in Figure 4(c). The SSITKA-MS experiment for plasmon-enhanced reaction condition is conducted following the same procedure with the dark counterpart except that green light irradiation is implemented throughout the experiment. The time-resolved DRIFT spectra and corresponding IR peak intensity evolutions are presented in Figure 4(g, h). Similar phenomena are observed in plasmon-enhanced reaction that the IR peaks of HCO$_3^*$, CO$_3^*$ shift to lower wavenumbers and the H^{12}COO* peak stays stable under plasmon-enhanced reaction condition. In MS plot (Figure 4(i)), it is noted that the decrease of ^{12}CO MS signal is faster in plasmon-enhanced reaction condition than the dark counterpart. To further verify the correlation between the light induced plasmonic enhancement with the surface life time of adsorbed species, a control group with green light power density of ~150 mW (60% of the full power used in Figure 4(g, h)) is conducted following the same SSITKA-MS protocol. The recorded DRIFT spectra and CO MS

17

1 signal evolution are presented in Figure 4(d, e) and (f). The corresponding mean surface lifetime

2 of $H^{12}CO_3^*$, $^{12}CO_3^*$ and $^{12}CO^*$($\tau_{HCO_3^*}$, $\tau_{CO_3^*}$ and τ_{CO^*}) are calculated and summarized in Table 1.

3 The details of derivation are described in SI-Section 4. The MS-CO decay profiles are plotted

4 together for a clear comparison as shown in Figure S8.

5

6 The SSITKA-MS experimental results can provide following insights. Firstly, the HCOO* can be

7 identified as the spectator in both the thermo- and plasmon-enhanced thermocatalytic reactions,

8 because IR peak of HCOO* shows no shift after switching from $^{12}CO_2$ to $^{13}CO_2$ in SSITKA-MS

9 experiments conducted in dark or green light irradiation (Figure 4). Secondly, the CO$_3^*$ and HCO$_3^*$

10 can be ruled out as the main reaction intermediates. As demonstrated in Table 1, the surface

11 residual time $\tau_{CO_3^*}$ and $\tau_{HCO_3^*}$ shows no correlation to the τ_{CO} [19]. Additionally, the $\tau_{CO_3^*}$ and

12 $\tau_{HCO_3^*}$ are not sensitive to the power density of incident light. Another control experiment with

13 $^{12}CO_2$/$^{13}CO_2$ isotope exchange in the absence of H_2 is conducted to further support this argument.

14 As shown in Figure S9, the IR peaks of CO$_3^*$ and HCO$_3^*$ also shift to lower wavenumber after

15 switching from $^{12}CO_2$ to $^{13}CO_2$ even without the involvement of H_2. This result indicates that the

16 CO$_3^*$ and HCO$_3^*$ adsorb weakly on the TiO$_2$. In summary, the HCOO*, HCO$_3^*$ and CO$_3^*$ are all

17 identified as the spectators and the redox reaction pathway is strongly suggested.
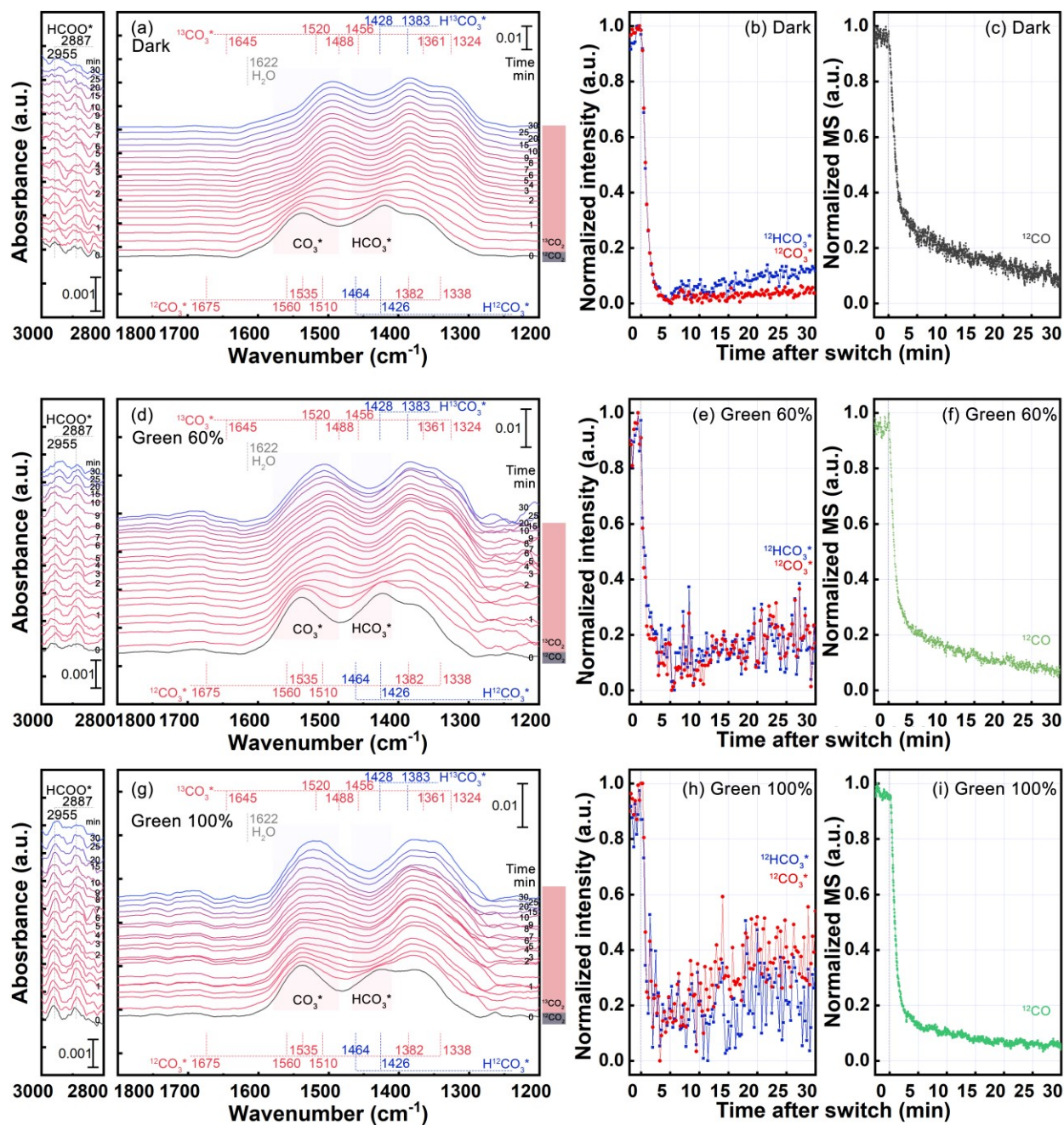
Figure 4. The operando-DRIFT spectra of Au/TiO$_2$ during SSITKA experiments under (a) dark, (d) green light with 60% power and (g) green light in full output, 200 °C. The corresponding time-resolved IR peak intensity decays of ^{12}HCO$_3$, ^{12}CO$_3$ in (b) dark, (e) 60% output green light and (h) full power green light. The corresponding ^{12}CO MS signal decays in (c) dark, (f) 60% power green light and (i) full power green light. ^{12}CO MS signal is measured with m/z =28. 0 min represents the moment ^{12}CO$_2$ is switched to ^{13}CO$_2$.

Table 1. Gas-phase (MS) and surface (IR absorbance band) kinetic mean surface lifetime of CO, CO_3^* and HCO_3^* derived from SSIKTA-MS experiments under different reaction conditions at 200 °C.

	GC	MS	IR	
	CO yield (μmol g_{cat}^{-1} s^{-1})	τ_{CO} (s)	$\tau_{CO_3^*}$ (s)	$\tau_{HCO_3^*}$ (s)
Dark	0.22	307.2±18.6	50.6±2.0	47.4±2.4
Green in 60% output (ND2)	0.45	231.0±7.8	45.1±5.4	44.8±6.6
Green in 100% output	0.70	185.4±27.6	42.0±8.4	45.6±14.4

3.4.3 Spontaneous dissociation of CO_2 on reduced Au/TiO_{2-x}

Another key evidence to support the redox mechanism of RWGS over Au/TiO_2 is that the CO_2 can be reduced by Au/TiO_{2-x} to CO without the assistance of $^*H$ (or H_2). The direct experimental evidence has not been reported before on Au/TiO_2. To provide a solid evidence of spontaneous dissociation of CO_2 to CO on Au/TiO_{2-x}, the isotope-labelled CO_2 adsorption experiments are conducted at both 30 and 200 °C. The catalysts are firstly *in-situ* treated with flowing air (30 sccm) at 400 °C for 30 min to remove the absorbed H^* and carbon species on the surface. Then the Au/TiO_2 catalysts are treated with flowing Ar (30 sccm) at 400 °C for another 30 min to create V_O [70, 71]. After cooling down, the $^{12}CO_2$ or $^{13}CO_2$ balanced in Ar is introduced and the surface species evolution is monitored by time-resolved DRIFTS. As shown in Figure 5(a), the peaks at 2176 and 2077 cm^{-1} emerge immediately after the $^{12}CO_2$ interacts with Au/TiO_{2-x}. These peaks are assigned to the ^{12}CO adsorption on the Ti^{4+} and $Au^{\delta-}$ sites of reduced Au/TiO_{2-x} surface. To rule out possible interventions from residual carbon, isotope labelled $^{13}CO_2$ is used and the corresponding DRIFT spectra are presented in Figure 5(b). Two peaks at 2138 and 2039 cm^{-1} ascribed to ^{13}CO show up, which match the theoretical frequency shift due to larger reduced mass (Equ. S6-S7 in SI-Section 3). More unambiguous spectroscopic evidence of dissociative adsorption of CO_2 on the Au/TiO_{2-x} is achieved at 30 °C with the same experimental procedure

1   (Figure 5(c, d)). The peaks at the same vibration frequency emerge with a higher intensity. Control

2   experiment (Figure S10) is conducted to rule out the possibility that CO^* might be derived from

3   the CO contaminant in CO_2 gas. The absence of CO^* during the CO_2 interaction with irreducible

4   Au/Al_2O_3 (Figure S10) suggests CO^* observed in Figure 5 is not from the contaminants but due to

5   the CO_2 dissociation with the replenishment of V_O on Au/TiO_{2-x}. Another control experiment of

6   CO_2 interaction with reduced TiO_{2-x} was presented in SI-Section 7 without observation of CO^*

7   either.
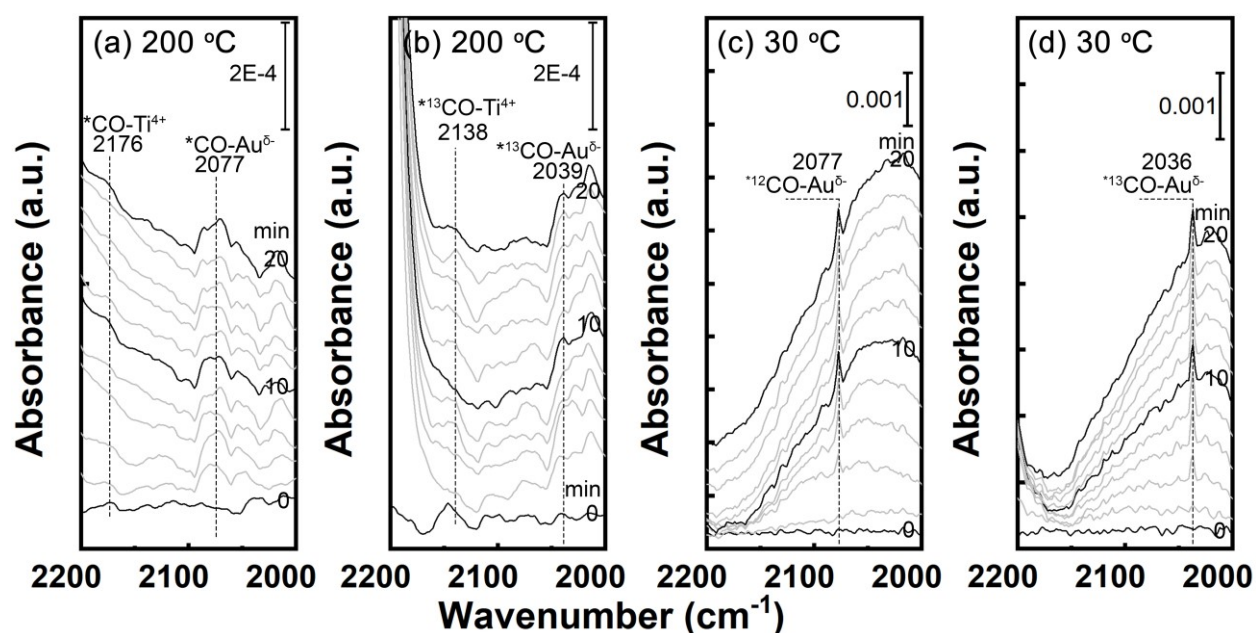
9   Figure 5. Time-resolved DRIFT spectra of CO_2 interaction with reduced Au/TiO_{2-x} in flowing Ar
10   with the absence of H_2: (a) $^{12}CO_2$ (b) $^{13}CO_2$ at 200 °C and (c) $^{12}CO_2$ (d) $^{13}CO_2$ at 30 °C.

11 **3.5   The inverse H/D kinetic isotope effects**

12   To further unravel reaction pathway and the plasmon-enhancement mechanism for CO_2

13   hydrogenation on Au/TiO_2, H/D kinetic isotope effects are measured at both dark and green-light

14   irradiation conditions at 200 to 400 °C (Figure 6). The inverse KIE, the ratio between reaction rate

15   using H_2 and D_2 smaller than 1, is observed on both dark and green irritation conditions at all

16   investigated temperature. At reaction temperature of 200, 250, 300, 400 °C, the KIE values are

1 0.56, 0.59, 0.61, 0.79 under dark and 0.61, 0.64, 0.72, 0.80 under green light irradiation,

2 respectively. Two results are worth notices: first, the KIE of reaction under green-light irradiation

3 condition always shows the higher value (closer to 1) than the counterpart in dark; Secondly, the

4 KIE value differences between reactions under green light irradiation and dark show an abrupt

5 drop to 0.01 at 400 °C. Since the overall apparent KIE can be a result combining the equilibrium

6 isotope effects (EIE) and KIE, spectrokinetic tests are conducted to determine the EIE of H/D

7 adsorbed on the surface. After annealing the Au/TiO_2 in H_2 (or D_2) balanced by Ar at 200 °C for

8 30 min, purging with Ar flow for 5 min can remove the gaseous H_2 (or D_2) from the reaction

9 chamber. After the introduction with CO_2, the $HCOO^*$ (or $DCOO^*$) formed on the surface is a

10 spectator and stable on the surface (Figure 4, SSITKA-MS experiments). As shown in Figure

11 S12(a, b), peak intensity of $HCOO^*$ and $DCOO^*$ located at 1571, 1568 cm^{-1} are compared [72].

12 The ratios of their absorbances are summarized in Figure S12(c), which represents the equilibrium

13 concentration of H^*/D^* on the surface. It confirms a positive EIE of ~1.5 at 200 and 300 °C, which

14 are not affected by the irradiation condition. In summary, based on the observed inverse apparent

15 H/D KIE and the normal EIE, the inverse KIE of the reaction is proven.

16

17 The observed inverse H/D KIE strongly supports the redox mechanism. If the elementary step

18 involving the bond formation/cleavage with H/D is the RDS, a normal KIE is expected, as reported

19 in the literature for Au based catalysts [73-75]. The inverse KIE can be plausibly explained by the

20 steric effects of H_2O^* adsorbed at the V_O site [76, 77]. The high energy (1.38 eV, Figure 7(a))

21 required for H_2O^* desorption for V_O generation indicates the H_2O^* desorption is another possible

22 rate-limiting step at low temperature. This argument is supported by the evolution of inverse KIE

23 value at higher temperature. At 400 °C when H_2O^* is not stable on the surface any more [78, 79],

1 an insignificant inverse KIE is observed, which indicates the RDS is irrelevant to H/D[*]. Under

2 green light irradiation, the KIE values are significantly shifted to 1, comparing with the

3 corresponding dark counterparts. It suggests that the light irradiation can significantly facilitate

4 the desorption of the H_2O^* and creation of V_O. The *ex-situ* ESR analyses (Figure 2) confirm that

5 more V_O is formed during the plasmon-enhanced RWGS reaction under green light irradiation than

6 in dark.
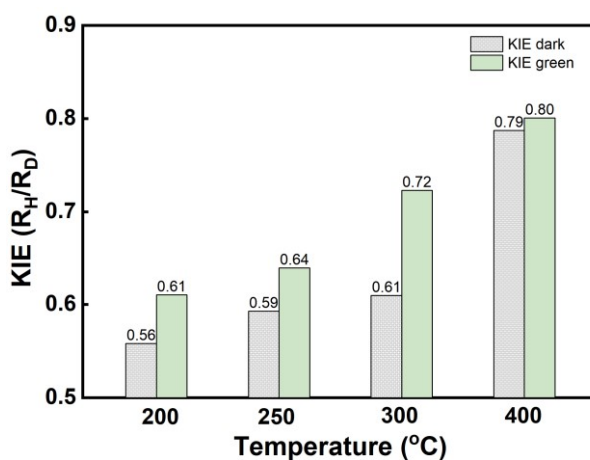
7

8 Figure 6. H_2/D_2 kinetic isotope effects of RWGS reaction under dark or green-light irradiation
9 condition at different temperature.

10

11 **3.6 The theoretical analyses of redox reaction pathway and the plasmonic**

12 **enhancement mechanism**

13 The redox mechanism is further supported by the DFT calculation results. The Au/TiO_2 catalysts

14 are modelled with an Au nanorod supported by anatase (101) surface, as illustration in Figure S14.

15 Unlike the Au nanocluster on rutile (110) facet most commonly used in the literature, the model

16 presented here is more suitable due to the following two considerations: (i) the anatase constitutes

17 ~80% of the commercial P25 TiO_2 used as the support for catalysts in the experiments; (ii) the

18 (101) facet is the most stable surface of anatase [80]. Anatase (101) facet is cleaved based on the

1 relaxed bulk structure and enlarged to a 2×3 supercell with 3 O-Ti-O trilayers. During the

2 calculation, the bottom O-Ti-O layer is fixed to mimic the bulk effects and the top 2 layers are free

3 to relax. The Au nanorod (32 atoms in total) is built in a structure of 3 layers, which are constituted

4 by 3, 3, 2 atoms in cross section, respectively. The Au nanorod axial direction is optimized in a

5 box with 15 Å vacuum space at the rest two directions. Then, the (111) surface of Au nanorod is

6 exposed at the Au/TiO_2 interface leaving a small residual compressive strain of 5.1% on Au

7 nanorod. It is similar to the reported value of 5.53% [81] and 3.7% [82]. A vacuum layer of 17 Å

8 is added for Au/TiO_2 slab model along Z-direction. Due to the supercell of Au/TiO_2 contains 248

9 atoms in total and possesses 20.8, 11.4 and 26.5 Å lattice constants along X, Y, Z direction

10 respectively, the gamma point sampling provides converged results.

11

12 Because the important role of V_O has been both confirmed by the experimental results in this work

13 as well as in the literature [6, 12], the redox and carboxyl pathways are compared at the V_O site.

14 As shown in Figure 7(a, b), the V_O creation is initialised with the heterolytic H_2 dissociation at the

15 perimeter site of Au/TiO_2 [50]. In our case, the adsorption energy of H_2 is calculated to be -0.11

16 eV and calculated activation energy (E_a) for H_2 dissociation is 0.46 eV, which is close to the

17 reported values determined by calculations [50, 81] and experiment [83]. The generation of H_2O^*

18 and V_O through the addition of H^* to the HO_{2C} site on the TiO_2 (101) surface exhibits an even

19 smaller E_a of 0.25 eV. In contrast to the two smaller E_a barriers for V_O formation, the desorption

20 of the H_2O^* from the V_O site is an endothermic process requiring a high energy of 1.38 eV. At V_O

21 site, the energy profiles of the two plausible pathways, direct CO_2 dissociation and carboxyl

22 formation, are compared. As shown in Figure 7(b), the most energy-favourable CO_2 adsorption at

23 the V_O sites is in bended configuration with the adsorption energy of -0.85 eV. The direct

dissociation of CO_2^* with the formation of CO^* on Au and replenishment of V_O exhibits the E_a of 0.65 eV. By contrast, the formation of $COOH^*$ at the V_O site requires an E_a of 0.96 eV, which is 1.48 times as large as the E_a of CO_2^* dissociation step. The calculation results suggest COOH pathway is less favourable than redox pathway. Although the DFT calculation results, inverse KIE and spontaneous CO_2 dissociation at 30 °C all suggest the redox mechanism is the main pathway, it is also worth mentioning that the COOH pathway is likely to be the minor reaction mechanism at 200 °C. In Figure 4, the MS-CO signal decays don't follow a perfect exponential function, which suggest a minor reaction pathway exists at 200 °C. Since we have completely ruled out the HCOO pathway, the most plausible candidate is the COOH pathway.

The light-enhanced V_O creation can be explained by the plasmonic hot electron indirect transfer model [84]: plasmonic hot electrons fill into the electron orbitals of adsorbed molecules. For Au/TiO_2, the schottky barrier smaller than 1 eV [85] is low enough for plasmon-excited hot electrons to overcome and inject into TiO_2 conduction band within a short timescale ~20 fs [86]. This physical model is verified by the *in-situ* IR spectra of CO adsorption on Au/TiO_2 under dark and green light irradiation (Figure S13). As shown in Figure S13, the blue-shift of CO-Au peak proves that the Au under green light irradiation is positively charged and the excited electrons inject into the TiO_2 support. Because H_2O^* desorption and CO_2^* dissociation are the two plausible RDSs, the electronic structure analyses of H_2O^* and CO_2^* adsorbed at V_O site of Au/TiO_{2-x} are conducted to provide insights on the roles of hot electrons. As shown in Figure 7(c, e), the crystal orbital Hamilton population (COHP) bonding analyses are conducted between the O atom in H_2O and two adjacent Ti atoms in TiO_2 slab. It can be seen that the antibonding states are very close to the E_F (0.16 eV above E_F). Especially for O-Ti2, there are major peaks of anti-bonding states

existing above the E_F within 2.34 eV (the photon energy of 530 nm green light). Comparatively, in the COHP analyses of CO_2^* at V_O site, the lowest unoccupied C-O1 antibonding state peak locates at 1.94 eV above the E_F (Figure 7(d, f)). Another possible plasmonic enhancement mechanism is the facilitated H_2 dissociation induced by hot electrons. However, since the molecular orbitals of H_2 only weakly couple with Au/TiO_2, the antibonding orbital is higher than ~2.5 eV above the E_F (Figure S15). In summary, the COHP analyses indicate the plasmonic hot electrons are more likely to fill into the antibonding orbitals of H_2O^* on Au/TiO_2 and significantly enhance its desorption. As the result, the V_O formation is remarkably promoted.
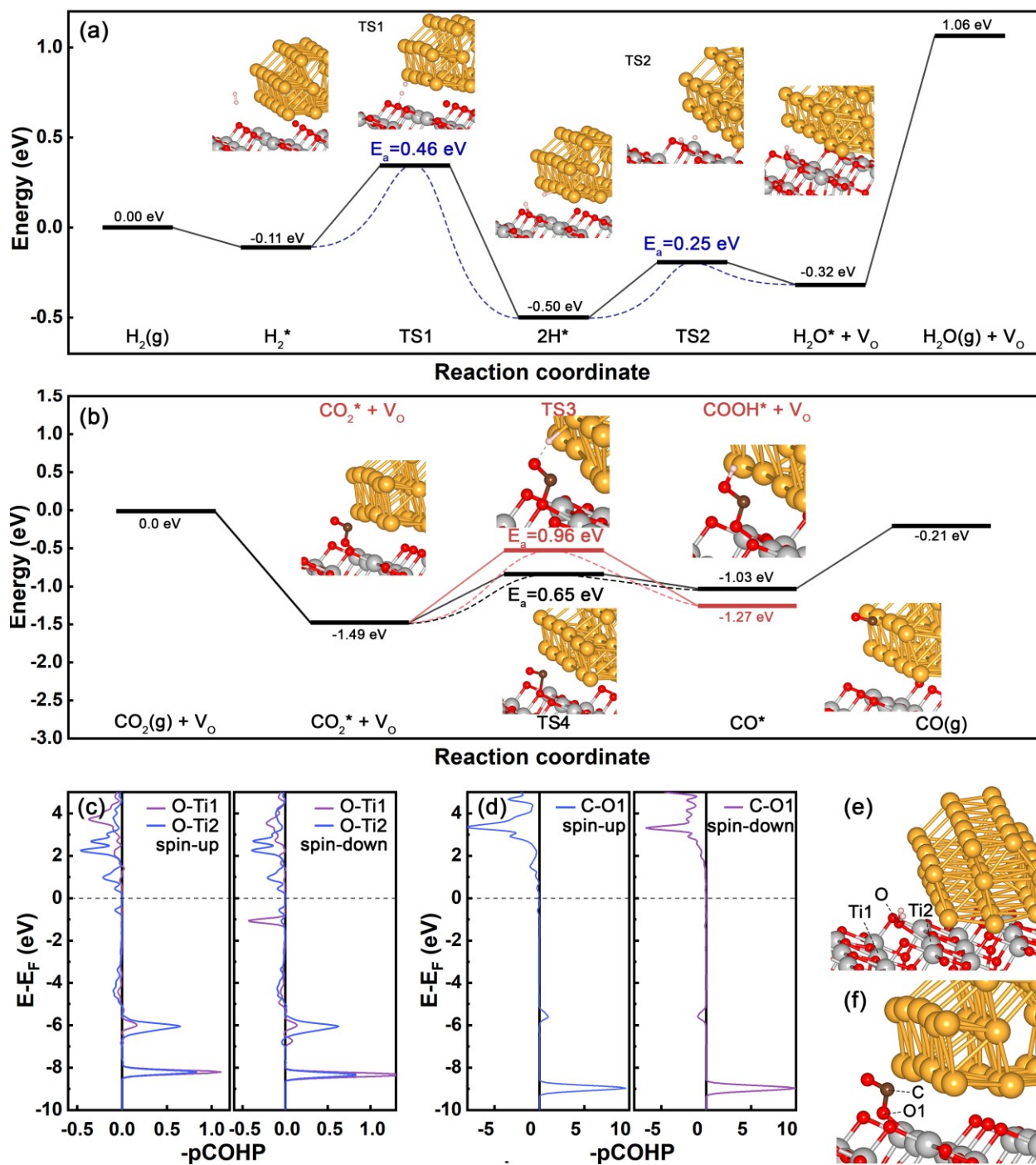
Figure 7. DFT calculated reaction profiles of (a) Au/TiO$_2$ reduction by H$_2$ with V$_O$ formation and (b) CO$_2$ conversion to CO via redox or carboxyl pathways. (c) pCOHP bonding analyses between O in H$_2$O* at V$_O$ site and two adjacent Ti atoms in TiO$_2$ slab. The corresponding configuration is shown in (e). (d) pCOHP bonding analyses of C-O in CO$_2^*$ at V$_O$ site of Au/TiO$_2$. The corresponding configuration is shown in (f). The negative and positive values of pCOHP represent the bonding and antibonding states, respectively. The amber, red, grey, brown and pink spheres represent Au, O, Ti, C and H atoms, respectively.

4 Conclusion

The redox mechanism is proven to be the main reaction pathway of CO_2 hydrogenation to CO reaction over Au/TiO_2 under both dark and green light irradiation conditions at 200 °C. The $HCOO^*$, HCO_3^* and CO_3^* observed in the *operando* DRIFT spectra are identified as the spectators based on SSITKA-MS experimental results. The isotope-labelled DRIFTS experiments demonstrate the dissociative adsorption of CO_2 at the V_O site of Au/TiO_{2-x} in the absence of H_2. Theoretical calculation and inverse H/D KIE further support the redox mechanism and suggest the RDS is likely to be the V_O creation step. Additionally, the facilitation of V_O formation is proven to be the main plasmonic enhancement mechanism by multiple experiments: *ex-situ* EPR spectroscopy analyses confirm a higher V_O concentration is formed during the reaction under green light irradiation; the H_2O IR peak is suppressed by light-irradiation during DRIFTS-MS experiments; the inverse KIE is significantly shifted to 1 under plasmonic enhancement. The COHP bonding analyses suggest the plasmonic hot electrons are most likely to transfer to the antibonding orbitals of H_2O^* adsorbed at the V_O site, which promotes the H_2O^* desorption and V_O formation. The insights on the mechanism of plasmonic promotion provided by this work can inspire the design of high-performance catalysts specific for photo-thermo coupled catalytic CO_2 conversion in the future.

1 (www.computecanada.ca). Mr. Fergus Dingwall is appreciated for the technical support in the

2 laboratory.

3

4

References:

[1] M.R. Allen, D.J. Frame, C. Huntingford, C.D. Jones, J.A. Lowe, M. Meinshausen, N. Meinshausen, Warming caused by cumulative carbon emissions towards the trillionth tonne, Nature, 458 (2009) 1163-1166. https://doi.org/10.1038/nature08019.

[2] Z.J. Wang, H. Song, H. Pang, Y.X. Ning, T.D. Dao, Z. Wang, H.L. Chen, Y.X. Weng, Q. Fu, T. Nagao, Y.M. Fang, J.H. Ye, Photo-assisted methanol synthesis via CO2 reduction under ambient pressure over plasmonic Cu/ZnO catalysts, Appl. Catal., B, 250 (2019) 10-16. https://doi.org/10.1016/j.apcatb.2019.03.003.

[3] L. Zhou, D.F. Swearer, C. Zhang, H. Robatjazi, H. Zhao, L. Henderson, L. Dong, P. Christopher, E.A. Carter, P. Nordlander, N.J. Halas, Quantifying hot carrier and thermal contributions in plasmonic photocatalysis, Science, 362 (2018) 69-72. https://doi.org/10.1126/science.aat6967.

[4] Z.J. Wang, H. Song, H. Liu, J. Ye, Coupling of Solar Energy and Thermal Energy for Carbon Dioxide Reduction: Status and Prospects, Angew. Chem., Int. Ed., 59 (2020) 8016-8035. https://doi.org/10.1002/anie.201907443.

[5] T.H. Tan, B.Q. Xie, Y.H. Ng, S.F.B. Abdullah, H.Y.M. Tang, N. Bedford, R.A. Taylor, K.F. Aguey-Zinsou, R. Amal, J. Scott, Unlocking the potential of the formate pathway in the photo-assisted Sabatier reaction, Nat. Catal., 3 (2020) 1034-1043. https://doi.org/10.1038/s41929-020-00544-3.

[6] L.F. Bobadilla, J.L. Santos, S. Ivanova, J.A. Odriozola, A. Urakawa, Unravelling the Role of Oxygen Vacancies in the Mechanism of the Reverse Water–Gas Shift Reaction by Operando DRIFTS and Ultraviolet–Visible Spectroscopy, ACS Catal., 8 (2018) 7455-7467. https://doi.org/10.1021/acscatal.8b02121.

[7] Y. Hartadi, D. Widmann, R.J. Behm, CO2 hydrogenation to methanol on supported Au catalysts under moderate reaction conditions: support and particle size effects, ChemSusChem, 8 (2015) 456-465. https://doi.org/10.1002/cssc.201402645.

[8] D.A. Panayotov, A.I. Frenkel, J.R. Morris, Catalysis and Photocatalysis by Nanoscale Au/TiO2: Perspectives for Renewable Energy, ACS Energy Lett., 2 (2017) 1223-1231. https://doi.org/10.1021/acsenergylett.7b00189.

[9] S. Li, P. Miao, Y. Zhang, J. Wu, B. Zhang, Y. Du, X. Han, J. Sun, P. Xu, Recent Advances in Plasmonic Nanostructures for Enhanced Photocatalysis and Electrocatalysis, Adv. Mater., (2020) e2000086. https://doi.org/10.1002/adma.202000086.

[10] L.C. Wang, M. Tahvildar Khazaneh, D. Widmann, R.J. Behm, TAP reactor studies of the oxidizing capability of CO2 on a Au/CeO2 catalyst – A first step toward identifying a redox mechanism in the Reverse Water–Gas Shift reaction, J. Catal., 302 (2013) 20-30. https://doi.org/10.1016/j.jcat.2013.02.021.

[11] L. Liu, C. Zhao, Y. Li, Spontaneous Dissociation of CO2 to CO on Defective Surface of Cu(I)/TiO2–x Nanoparticles at Room Temperature, J. Phys. Chem. C, 116 (2012) 7904-7912. https://doi.org/10.1021/jp300932b.

[12] X. Yang, S. Kattel, S.D. Senanayake, J.A. Boscoboinik, X. Nie, J. Graciani, J.A. Rodriguez, P. Liu, D.J. Stacchiola, J.G. Chen, Low Pressure CO2 Hydrogenation to Methanol over Gold Nanoparticles Activated on a CeO(x)/TiO2 Interface, J. Am. Chem. Soc., 137 (2015) 10104-10107. https://doi.org/10.1021/jacs.5b06150.

[13] F.C. Meunier, D. Tibiletti, A. Goguet, D. Reid, R. Burch, On the reactivity of carbonate species on a Pt/CeO2 catalyst under various reaction atmospheres: Application of the isotopic

exchange technique, Appl. Catal., A, 289 (2005) 104-112. https://doi.org/10.1016/j.apcata.2005.04.018.

[14] A. Goguet, F.C. Meunier, D. Tibiletti, J.P. Breen, R. Burch, Spectrokinetic Investigation of Reverse Water-Gas-Shift Reaction Intermediates over a Pt/CeO2Catalyst, J. Phys. Chem. B, 108 (2004) 20240-20246. https://doi.org/10.1021/jp047242w.

[15] X. Chen, X. Su, B. Liang, X. Yang, X. Ren, H. Duan, Y. Huang, T. Zhang, Identification of relevant active sites and a mechanism study for reverse water gas shift reaction over Pt/CeO 2 catalysts, Journal of Energy Chemistry, 25 (2016) 1051-1057. https://doi.org/10.1016/j.jechem.2016.11.011.

[16] X. Wang, H. Shi, J.H. Kwak, J. Szanyi, Mechanism of CO2 Hydrogenation on Pd/Al2O3 Catalysts: Kinetics and Transient DRIFTS-MS Studies, ACS Catal., 5 (2015) 6337-6349. https://doi.org/10.1021/acscatal.5b01464.

[17] A.A. Upadhye, I. Ro, X. Zeng, H.J. Kim, I. Tejedor, M.A. Anderson, J.A. Dumesic, G.W. Huber, Plasmon-enhanced reverse water gas shift reaction over oxide supported Au catalysts, Catal. Sci. Technol., 5 (2015) 2590-2601. https://doi.org/10.1039/c4cy01183j.

[18] J.A. Rodriguez, S. Ma, P. Liu, J. Hrbek, J. Evans, M. Perez, Activity of CeOx and TiOx nanoparticles grown on Au(111) in the water-gas shift reaction, Science, 318 (2007) 1757-1760. https://doi.org/10.1126/science.1150038.

[19] N.C. Nelson, M.T. Nguyen, V.A. Glezakou, R. Rousseau, J. Szanyi, Carboxyl intermediate formation via an in situ-generated metastable active site during water-gas shift catalysis, Nat. Catal., 2 (2019) 916-924. https://doi.org/10.1038/s41929-019-0343-2.

[20] X. Zhang, X. Li, D. Zhang, N.Q. Su, W. Yang, H.O. Everitt, J. Liu, Product selectivity in plasmonic photocatalysis for carbon dioxide hydrogenation, Nat. Commun., 8 (2017) 14542. https://doi.org/10.1038/ncomms14542.

[21] X.Q. Li, H.O. Everitt, J. Liu, Confirming nonthermal plasmonic effects enhance CO2 methanation on Rh/TiO2 catalysts, Nano Res., 12 (2019) 1906-1911. https://doi.org/10.1007/s12274-019-2457-x.

[22] S. Ullah, E. Lovell, R.J. Wong, T.H. Tan, J.A. Scott, R. Amal, Light-Enhanced CO2 Reduction to CH4 using Nonprecious Transition-Metal Catalysts, ACS Sustainable Chem. Eng., 8 (2020) 5056-5066. https://doi.org/10.1021/acssuschemeng.9b06823.

[23] L.A. Zhou, J.M.P. Martirez, J. Finzel, C. Zhang, D.F. Swearer, S. Tian, H. Robatjazi, M.H. Lou, L.L. Dong, L. Henderson, P. Christopher, E.A. Carter, P. Nordlander, N.J. Halas, Light-driven methane dry reforming with single atomic site antenna-reactor plasmonic photocatalysts, Nature Energy, 5 (2020) 61-70. https://doi.org/10.1038/s41560-019-0517-9.

[24] L. Lin, K. Wang, K. Yang, X. Chen, X. Fu, W. Dai, The visible-light-assisted thermocatalytic methanation of CO2 over Ru/TiO(2-x)Nx, Appl. Catal., B, 204 (2017) 440-455. https://doi.org/10.1016/j.apcatb.2016.11.054.

[25] B. Xie, R.J. Wong, T.H. Tan, M. Higham, E.K. Gibson, D. Decarolis, J. Callison, K.F. Aguey-Zinsou, M. Bowker, C.R.A. Catlow, J. Scott, R. Amal, Synergistic ultraviolet and visible light photo-activation enables intensified low-temperature methanol synthesis over copper/zinc oxide/alumina, Nat. Commun., 11 (2020) 1615. https://doi.org/10.1038/s41467-020-15445-z.

[26] Y. Zhang, S. He, W. Guo, Y. Hu, J. Huang, J.R. Mulcahy, W.D. Wei, Surface-Plasmon-Driven Hot Electron Photochemistry, Chem. Rev., 118 (2018) 2927-2954. https://doi.org/10.1021/acs.chemrev.7b00430.

[27] U. Aslam, V.G. Rao, S. Chavez, S. Linic, Catalytic conversion of solar to chemical energy on plasmonic metal nanostructures, Nat. Catal., 1 (2018) 656-665. https://doi.org/10.1038/s41929-018-0138-x.

[28] H. Liu, T.D. Dao, L. Liu, X. Meng, T. Nagao, J. Ye, Light assisted CO 2 reduction with methane over group VIII metals: Universality of metal localized surface plasmon resonance in reactant activation, Appl. Catal., B, 209 (2017) 183-189. https://doi.org/10.1016/j.apcatb.2017.02.080.

[29] P. Giannozzi, S. Baroni, N. Bonini, M. Calandra, R. Car, C. Cavazzoni, D. Ceresoli, G.L. Chiarotti, M. Cococcioni, I. Dabo, A. Dal Corso, S. de Gironcoli, S. Fabris, G. Fratesi, R. Gebauer, U. Gerstmann, C. Gougoussis, A. Kokalj, M. Lazzeri, L. Martin-Samos, N. Marzari, F. Mauri, R. Mazzarello, S. Paolini, A. Pasquarello, L. Paulatto, C. Sbraccia, S. Scandolo, G. Sclauzero, A.P. Seitsonen, A. Smogunov, P. Umari, R.M. Wentzcovitch, QUANTUM ESPRESSO: a modular and open-source software project for quantum simulations of materials, J. Phys. Condens. Matter., 21 (2009) 395502. https://doi.org/10.1088/0953-8984/21/39/395502.

[30] P. Giannozzi, O. Andreussi, T. Brumme, O. Bunau, M. Buongiorno Nardelli, M. Calandra, R. Car, C. Cavazzoni, D. Ceresoli, M. Cococcioni, N. Colonna, I. Carnimeo, A. Dal Corso, S. de Gironcoli, P. Delugas, R.A. DiStasio, A. Ferretti, A. Floris, G. Fratesi, G. Fugallo, R. Gebauer, U. Gerstmann, F. Giustino, T. Gorni, J. Jia, M. Kawamura, H.Y. Ko, A. Kokalj, E. Kucukbenli, M. Lazzeri, M. Marsili, N. Marzari, F. Mauri, N.L. Nguyen, H.V. Nguyen, A. Otero-de-la-Roza, L. Paulatto, S. Ponce, D. Rocca, R. Sabatini, B. Santra, M. Schlipf, A.P. Seitsonen, A. Smogunov, I. Timrov, T. Thonhauser, P. Umari, N. Vast, X. Wu, S. Baroni, Advanced capabilities for materials modelling with Quantum ESPRESSO, J. Phys. Condens. Matter., 29 (2017) 465901. https://doi.org/10.1088/1361-648X/aa8f79.

[31] J.P. Perdew, K. Burke, M. Ernzerhof, Generalized Gradient Approximation Made Simple, Phys. Rev. Lett., 77 (1996) 3865-3868. https://doi.org/10.1103/PhysRevLett.77.3865.

[32] K.F. Garrity, J.W. Bennett, K.M. Rabe, D. Vanderbilt, Pseudopotentials for high-throughput DFT calculations, Comput. Mater. Sci., 81 (2014) 446-452. https://doi.org/10.1016/j.commatsci.2013.08.053.

[33] X. Ma, Y. Dai, M. Guo, B. Huang, Relative photooxidation and photoreduction activities of the {100}, {101}, and {001} surfaces of anatase TiO_2, Langmuir, 29 (2013) 13647-13654. https://doi.org/10.1021/la403351v.

[34] M. Farnesi Camellone, J. Zhao, L. Jin, Y. Wang, M. Muhler, D. Marx, Molecular understanding of reactivity and selectivity for methanol oxidation at the Au/TiO_2 interface, Angew. Chem., Int. Ed., 52 (2013) 5780-5784. https://doi.org/10.1002/anie.201301868.

[35] B.J. Morgan, G.W. Watson, Intrinsic n-type Defect Formation in TiO_2: A Comparison of Rutile and Anatase from GGA plus U Calculations, J. Phys. Chem. C, 114 (2010) 2321-2328. https://doi.org/10.1021/jp9088047.

[36] M. Cococcioni, S. de Gironcoli, Linear response approach to the calculation of the effective interaction parameters in theLDA+Umethod, Phys. Rev. B, 71 (2005) 035105. https://doi.org/10.1103/PhysRevB.71.035105.

[37] S. Grimme, J. Antony, S. Ehrlich, H. Krieg, A consistent and accurate ab initio parametrization of density functional dispersion correction (DFT-D) for the 94 elements H-Pu, J. Chem. Phys., 132 (2010) 154104. https://doi.org/10.1063/1.3382344.

[38] S. Smidstrup, A. Pedersen, K. Stokbro, H. Jonsson, Improved initial guess for minimum energy path calculations, J. Chem. Phys., 140 (2014) 214106. https://doi.org/10.1063/1.4878664.

[39] K. Momma, F. Izumi, VESTA 3for three-dimensional visualization of crystal, volumetric and morphology data, J. Appl. Crystallogr., 44 (2011) 1272-1276. https://doi.org/10.1107/s0021889811038970.

[40] S. Maintz, V.L. Deringer, A.L. Tchougreeff, R. Dronskowski, LOBSTER: A tool to extract chemical bonding from plane-wave based DFT, J. Comput. Chem., 37 (2016) 1030-1035. https://doi.org/10.1002/jcc.24300.

[41] A. Dal Corso, Pseudopotentials periodic table: From H to Pu, Comput. Mater. Sci., 95 (2014) 337-350. https://doi.org/10.1016/j.commatsci.2014.07.043.

[42] J.B. Priebe, J. Radnik, A.J.J. Lennox, M.-M. Pohl, M. Karnahl, D. Hollmann, K. Grabow, U. Bentrup, H. Junge, M. Beller, A. Brückner, Solar Hydrogen Production by Plasmonic Au–TiO2 Catalysts: Impact of Synthesis Protocol and TiO2 Phase on Charge Transfer Efficiency and H2 Evolution Rates, ACS Catal., 5 (2015) 2137-2148. https://doi.org/10.1021/cs5018375.

[43] K. Qian, B.C. Sweeny, A.C. Johnston-Peck, W. Niu, J.O. Graham, J.S. DuChene, J. Qiu, Y.C. Wang, M.H. Engelhard, D. Su, E.A. Stach, W.D. Wei, Surface plasmon-driven water reduction: gold nanoparticle size matters, J. Am. Chem. Soc., 136 (2014) 9842-9845. https://doi.org/10.1021/ja504097v.

[44] V. Jovic, W.-T. Chen, D. Sun-Waterhouse, M.G. Blackford, H. Idriss, G.I.N. Waterhouse, Effect of gold loading and TiO2 support composition on the activity of Au/TiO2 photocatalysts for H2 production from ethanol–water mixtures, J. Catal., 305 (2013) 307-317. https://doi.org/10.1016/j.jcat.2013.05.031.

[45] M. Kotobuki, R. Leppelt, D.A. Hansgen, D. Widmann, R.J. Behm, Reactive oxygen on a Au/TiO2 supported catalyst, J. Catal., 264 (2009) 67-76. https://doi.org/10.1016/j.jcat.2009.03.013.

[46] G. Baffou, I. Bordacchini, A. Baldi, R. Quidant, Simple experimental procedures to distinguish photothermal from hot-carrier processes in plasmonics, Light: Sci. Appl., 9 (2020) 108. https://doi.org/10.1038/s41377-020-00345-0.

[47] A. Naldoni, M. Allieta, S. Santangelo, M. Marelli, F. Fabbri, S. Cappelli, C.L. Bianchi, R. Psaro, V. Dal Santo, Effect of Nature and Location of Defects on Bandgap Narrowing in Black TiO2 Nanoparticles, J. Am. Chem. Soc., 134 (2012) 7600-7603. https://doi.org/10.1021/ja3012676.

[48] X. Zhou, E. Wierzbicka, N. Liu, P. Schmuki, Black and white anatase, rutile and mixed forms: band-edges and photocatalytic activity, Chem. Commun., 55 (2019) 533-536. https://doi.org/10.1039/c8cc07665k.

[49] J.-Y. Shin, J.H. Joo, D. Samuelis, J. Maier, Oxygen-Deficient TiO2−δ Nanoparticles via Hydrogen Reduction for High Rate Capability Lithium Batteries, Chem. Mater., 24 (2012) 543-551. https://doi.org/10.1021/cm2031009.

[50] K. Sun, M. Kohyama, S. Tanaka, S. Takeda, A Study on the Mechanism for H2 Dissociation on Au/TiO2 Catalysts, J. Phys. Chem. C, 118 (2014) 1611-1617. https://doi.org/10.1021/jp4099254.

[51] A. Ruiz Puigdollers, P. Schlexer, S. Tosoni, G. Pacchioni, Increasing Oxide Reducibility: The Role of Metal/Oxide Interfaces in the Formation of Oxygen Vacancies, ACS Catal., 7 (2017) 6493-6513. https://doi.org/10.1021/acscatal.7b01913.

[52] K. Wang, J. Lu, Y. Lu, C.H. Lau, Y. Zheng, X. Fan, Unravelling the C C coupling in CO2 photocatalytic reduction with H2O on Au/TiO2-x: Combination of plasmonic excitation and oxygen vacancy, Appl. Catal., B, 292 (2021) 120147. https://doi.org/10.1016/j.apcatb.2021.120147.

[53] H. Liu, H.T. Ma, X.Z. Li, W.Z. Li, M. Wu, X.H. Bao, The enhancement of TiO2 photocatalytic activity by hydrogen thermal treatment, Chemosphere, 50 (2003) 39-46. https://doi.org/10.1016/s0045-6535(02)00486-1.

[54] M. Okumura, J.M. Coronado, J. Soria, M. Haruta, J.C. Conesa, EPR Study of CO and O2 Interaction with Supported Au Catalysts, J. Catal., 203 (2001) 168-174. https://doi.org/10.1006/jcat.2001.3307.

[55] X. Zou, J. Liu, J. Su, F. Zuo, J. Chen, P. Feng, Facile synthesis of thermal- and photostable titania with paramagnetic oxygen vacancies for visible-light photocatalysis, Chem. - Eur. J., 19 (2013) 2866-2873. https://doi.org/10.1002/chem.201202833.

[56] J.B. Priebe, M. Karnahl, H. Junge, M. Beller, D. Hollmann, A. Bruckner, Water reduction with visible light: synergy between optical transitions and electron transfer in Au-TiO(2) catalysts visualized by in situ EPR spectroscopy, Angew. Chem., Int. Ed., 52 (2013) 11420-11424. https://doi.org/10.1002/anie.201306504.

[57] B. Choudhury, A. Choudhury, Room temperature ferromagnetism in defective TiO2 nanoparticles: Role of surface and grain boundary oxygen vacancies, J. Appl. Phys., 114 (2013). https://doi.org/10.1063/1.4833562.

[58] K. Tanaka, J.M. White, Characterization of Species Adsorbed on Oxidized and Reduced Anatase, J. Phys. Chem., 86 (1982) 4708-4714. https://doi.org/DOI 10.1021/j100221a014.

[59] S. Wei, W.W. Wang, X.P. Fu, S.Q. Li, C.J. Jia, The effect of reactants adsorption and products desorption for Au/TiO2 in catalyzing CO oxidation, J. Catal., 376 (2019) 134-145. https://doi.org/10.1016/j.jcat.2019.06.038.

[60] Y. Denkwitz, Z. Zhao, U. Hormann, U. Kaiser, V. Plzak, R. Behm, Stability and deactivation of unconditioned Au/TiO2 catalysts during CO oxidation in a near-stoichiometric and O2-rich reaction atmosphere, J. Catal., 251 (2007) 363-373. https://doi.org/10.1016/j.jcat.2007.07.029.

[61] S. Gaur, H. Wu, G.G. Stanley, K. More, C.S.S.R. Kumar, J.J. Spivey, CO oxidation studies over cluster-derived Au/TiO2 and AUROlite™ Au/TiO2 catalysts using DRIFTS, Catal. Today, 208 (2013) 72-81. https://doi.org/10.1016/j.cattod.2012.10.029.

[62] G.H. Yin, X.Y. Huang, T.Y. Chen, W. Zhao, Q.Y. Bi, J. Xu, Y.F. Han, F.Q. Huang, Hydrogenated Blue Titania for Efficient Solar to Chemical Conversions: Preparation, Characterization, and Reaction Mechanism of CO2 Reduction, ACS Catal., 8 (2018) 1009-1017. https://doi.org/10.1021/acscatal.7b03473.

[63] J. Baltrusaitis, J. Schuttlefield, E. Zeitler, V.H. Grassian, Carbon dioxide adsorption on oxide nanoparticle surfaces, Chem. Eng. J., 170 (2011) 471-481. https://doi.org/10.1016/j.cej.2010.12.041.

[64] L.C. Liu, X.R. Gu, Y. Cao, X.J. Yao, L. Zhang, C.J. Tang, F. Gao, L. Dong, Crystal-Plane Effects on the Catalytic Properties of Au/TiO2, ACS Catal., 3 (2013) 2768-2775. https://doi.org/10.1021/cs400492w.

[65] T. Kecskes, J. Rasko, J. Kiss, FTIR and mass spectrometric study of HCOOH interaction with TiO2 supported Rh and Au catalysts, Appl. Catal., A, 268 (2004) 9-16. https://doi.org/10.1016/j.apcata.2004.03.021.

[66] K.L. Miller, C.W. Lee, J.L. Falconer, J.W. Medlin, Effect of water on formic acid photocatalytic decomposition on TiO2 and Pt/TiO2, J. Catal., 275 (2010) 294-299. https://doi.org/10.1016/j.jcat.2010.08.011.

[67] M. El-Maazawi, A.N. Finken, A.B. Nair, V.H. Grassian, Adsorption and photocatalytic oxidation of acetone on TiO2: An in situ transmission FT-IR study, J. Catal., 191 (2000) 138-146. https://doi.org/DOI 10.1006/jcat.1999.2794.

[68] M. Sridhar, D. Ferri, M. Elsener, J.A. van Bokhoven, O. Krocher, Promotion of Ammonium Formate and Formic Acid Decomposition over Au/TiO2 by Support Basicity under SCR-Relevant Conditions, ACS Catal., 5 (2015) 4772-4782. https://doi.org/10.1021/acscatal.5b01057.

[69] L. Mino, Á. Morales-García, S.T. Bromley, F. Illas, Understanding the nature and location of hydroxyl groups on hydrated titania nanoparticles, Nanoscale, 13 (2021) 6577-6585. https://doi.org/10.1039/d1nr00610j.

[70] L.J. Liu, Y.Q. Jiang, H.L. Zhao, J.T. Chen, J.L. Cheng, K.S. Yang, Y. Li, Engineering Coexposed {001} and {101} Facets in Oxygen-Deficient TiO2 Nanocrystals for Enhanced CO2 Photoreduction under Visible Light, ACS Catal., 6 (2016) 1097-1108. https://doi.org/10.1021/acscatal.5b02098.

[71] L.J. Liu, H.L. Zhao, J.M. Andino, Y. Li, Photocatalytic CO2 Reduction with H2O on TiO2 Nanocrystals: Comparison of Anatase, Rutile, and Brookite Polymorphs and Exploration of Surface Chemistry, ACS Catal., 2 (2012) 1817-1828. https://doi.org/10.1021/cs300273q.

[72] M. El-Roz, P. Bazin, M. Daturi, F. Thibault-Starzyk, On the mechanism of methanol photooxidation to methylformate and carbon dioxide on TiO2: an operando-FTIR study, Phys. Chem. Chem. Phys., 17 (2015) 11277-11283. https://doi.org/10.1039/c5cp00726g.

[73] I.X. Green, W. Tang, M. Neurock, J.T. Yates, Jr., Low-temperature catalytic H2 oxidation over Au nanoparticle/TiO2 dual perimeter sites, Angew. Chem., Int. Ed., 50 (2011) 10186-10189. https://doi.org/10.1002/anie.201101612.

[74] A. Rezvani, A.M. Abdel-Mageed, T. Ishida, T. Murayama, M. Parlinska-Wojtan, R.J. Behm, CO2 Reduction to Methanol on Au/CeO2 Catalysts: Mechanistic Insights from Activation/Deactivation and SSITKA Measurements, ACS Catal., 10 (2020) 3580-3594. https://doi.org/10.1021/acscatal.9b04655.

[75] Y. Bai, B.W.J. Chen, G. Peng, M. Mavrikakis, Density functional theory study of thermodynamic and kinetic isotope effects of H2/D2 dissociative adsorption on transition metals, Catal. Sci. Technol., 8 (2018) 3321-3335. https://doi.org/10.1039/c8cy00878g.

[76] A.K. Soper, C.J. Benmore, Quantum Differences between Heavy and Light Water, Phys. Rev. Lett., 101 (2008) 065502. https://doi.org/10.1103/PhysRevLett.101.065502.

[77] E.C.M. Tse, T.T.H. Hoang, J.A. Varnell, A.A. Gewirth, Observation of an Inverse Kinetic Isotope Effect in Oxygen Evolution Electrochemistry, ACS Catal., 6 (2016) 5706-5714. https://doi.org/10.1021/acscatal.6b01170.

[78] D.D. Beck, J.M. White, C.T. Ratcliffe, Catalytic reduction of carbon monoxide with hydrogen sulfide. 2. Adsorption of water and hydrogen sulfide on anatase and rutile, J. Phys. Chem., 90 (1986) 3123-3131. https://doi.org/10.1021/j100405a018.

[79] M. Egashira, S. Kawasumi, S. Kagawa, T. Seiyama, Temperature Programmed Desorption Study of Water Adsorbed on Metal Oxides. I. Anatase and Rutile, Bull. Chem. Soc. Jpn., 51 (1978) 3144-3149. https://doi.org/10.1246/bcsj.51.3144.

[80] J.-Y. Liu, X.-Q. Gong, A.N. Alexandrova, Mechanism of CO2 Photocatalytic Reduction to Methane and Methanol on Defected Anatase TiO2 (101): A Density Functional Theory Study, J. Phys. Chem. C, 123 (2019) 3505-3511. https://doi.org/10.1021/acs.jpcc.8b09539.

[81] T. Whittaker, K.B.S. Kumar, C. Peterson, M.N. Pollock, L.C. Grabow, B.D. Chandler, H2 Oxidation over Supported Au Nanoparticle Catalysts: Evidence for Heterolytic H2 Activation at the Metal–Support Interface, J. Am. Chem. Soc., 140 (2018) 16469-16487. https://doi.org/10.1021/jacs.8b04991.

[82] Z. Duan, G. Henkelman, CO Oxidation at the Au/TiO2 Boundary: The Role of the Au/Ti5c Site, ACS Catal., 5 (2015) 1589-1595. https://doi.org/10.1021/cs501610a.

[83] B. Yang, X.M. Cao, X.Q. Gong, P. Hu, A density functional theory study of hydrogen dissociation and diffusion at the perimeter sites of Au/TiO2, Phys. Chem. Chem. Phys., 14 (2012) 3741-3745. https://doi.org/10.1039/c2cp23755e.

[84] S. Mukherjee, F. Libisch, N. Large, O. Neumann, L.V. Brown, J. Cheng, J.B. Lassiter, E.A. Carter, P. Nordlander, N.J. Halas, Hot electrons do the impossible: plasmon-induced dissociation of H2 on Au, Nano Lett., 13 (2013) 240-247. https://doi.org/10.1021/nl303940z.

[85] M.S. Arshad, S. Trafela, K.Z. Rozman, J. Kovac, P. Djinovic, A. Pintar, Determination of Schottky barrier height and enhanced photoelectron generation in novel plasmonic immobilized multisegmented (Au/TiO2) nanorod arrays (NRAs) suitable for solar energy conversion applications, J. Mater. Chem. C, 5 (2017) 10509-10516. https://doi.org/10.1039/c7tc02633a.

[86] C. Clavero, Plasmon-induced hot-electron generation at nanoparticle/metal-oxide interfaces for photovoltaic and photocatalytic devices, Nature Photonics, 8 (2014) 95-103. https://doi.org/10.1038/Nphoton.2013.238.